

# Operando Photoelectron Spectroscopy Analysis of Li<sub>6</sub>PS<sub>5</sub>Cl Electrochemical Decomposition Reactions in Solid-State Batteries

Burak Aktekin<sup>1,2\*†</sup>, Elmar Kataev<sup>3,4\*†</sup>, Luise M. Riegger<sup>1,2</sup>, Raul Garcia-Diez<sup>3,4</sup>, Zora Chalkley<sup>3,4</sup>, Juri Becker<sup>1,2</sup>, Regan G. Wilks<sup>3,4</sup>, Anja Henss<sup>1,2</sup>, Marcus Bär<sup>3,4,5,6\*</sup>, Jürgen Janek<sup>1,2\*</sup>

<sup>1</sup>*Institute of Physical Chemistry, Justus-Liebig-Universität Giessen, D-35392 Giessen, Germany*

<sup>2</sup>*Center for Materials Research, Justus-Liebig-Universität Giessen, D-35392 Giessen, Germany*

<sup>3</sup>*Department of Interface Design, Helmholtz-Zentrum Berlin für Materialien und Energie GmbH (HZB), D-12489 Berlin, Germany*

<sup>4</sup>*Energy Materials In-Situ Laboratory Berlin (EMIL), HZB, D-12489 Berlin, Germany*

<sup>5</sup>*Lehrstuhl für Physikalische Chemie II, Friedrich-Alexander-Universität Erlangen-Nürnberg (FAU), D-91058 Erlangen, Germany*

<sup>6</sup>*Department of X-ray Spectroscopy at Interfaces of Thin Films, Helmholtz-Institute Erlangen-Nürnberg for Renewable Energy (HI ERN), Berlin, Germany*

\*burak.aktekin@phys.chemie.uni-giessen.de, elmar.kataev@helmholtz-berlin.de

\*marcus.baer@helmholtz-berlin.de, juergen.janek@phys.chemie.uni-giessen.de

†These authors contributed equally.

---

**Abstract.** It is crucial to understand at which potentials electrolyte decomposition reactions start and which chemical species are present in the subsequently formed decomposition films, e.g., solid electrolyte interphase (SEI). Herein, a new operando experimental approach is introduced to investigate such reactions by employing hard X-ray photoelectron spectroscopy (HAXPES). This approach enables the examination of the SEI formed below a thin metal film (e.g., 6 nm nickel) acting as the working electrode in an electrochemical cell with sulfide-based Li<sub>6</sub>PS<sub>5</sub>Cl solid electrolyte. Electrolyte reduction reactions already start at 1.75 V (vs. Li<sup>+</sup>/Li) and result in considerable Li<sub>2</sub>S formation, particularly in the voltage range of 1.5 – 1.0 V. A heterogeneous/layered microstructure of the SEI is observed (e.g., preferential Li<sub>2</sub>O and Li<sub>2</sub>S deposition near the current collector). The reversibility of side reactions is also observed, as Li<sub>2</sub>O and Li<sub>2</sub>S decompose in the 2–4 V potential window, generating oxidized sulfur species, sulfites and sulfates.

---

**Keywords:** HAXPES, operando, lithium metal anode, LPSCL, solid electrolytes, SEI, sulfide electrolyte

## Introduction

Today, lithium-ion batteries (LiBs) are taking a central position in the electrification of transportation.<sup>1</sup> In order to accelerate the transition away from fossil fuels in the transportation sector, it is crucial to have advanced battery technologies offering high specific energy and power, while also being cost-effective, safe, and environmentally friendly.<sup>2</sup> All-solid-state batteries (ASSBs) represent a promising battery technology that can achieve high-energy densities due to their advantages such as the potential for bipolar stacking, ability to utilize

high-energy-density electrodes (e.g., lithium metal) and their projected safety.<sup>3</sup> Unfortunately, most solid electrolytes (SEs) are not electrochemically stable at low potentials, e.g., at the operation potential of high-energy-density lithium metal and silicon anodes (i.e., negative electrodes).<sup>4</sup> Therefore, electrolyte reduction reactions occur at the anode|SE interface, forming either a solid electrolyte interphase (SEI) or a mixed conducting interphase (MCI) due to accumulation of decomposition products.<sup>5–8</sup> Electrolyte reduction reactions, and the succeeding interphase formation, will cause lithium inventory losses<sup>9</sup> and impede the lithium transport kinetics at the anode|SE

interface,<sup>5,10</sup> both leading to poor battery cycle life. Thus, it is crucial to determine the onset potential of different side reactions and reaction products through theoretical studies.<sup>4,11,12</sup> However, it is also quite important to experimentally determine onset potentials and reaction products since the actual chemical behavior may vary under practically relevant conditions. This knowledge is key to designing improved anode|SE interphases and thereby better performing battery systems.

Sulfide-based materials are very promising SE candidates because of their high ionic conductivities reaching that of industrial liquid electrolytes (10 mS cm<sup>-1</sup>) and ability for sintering at room temperature, making them attractive as compared to oxide-based SEs.<sup>4</sup> However, the implementation of sulfide-based SEs into ASSBs has challenges, particularly when used with high-energy-density anodes such as lithium metal which operates at the potential  $E_{\text{H}}(\text{Li}^+/\text{Li}) = 0 \text{ V}$  (i.e.  $-3.04 \text{ V}$  vs. the standard hydrogen electrode). The electrolyte stability window of sulfide SEs ranges between 1.5 – 2.5 V vs.  $\text{Li}^+/\text{Li}$ , and electrolyte reduction reactions are predicted to occur at potentials below the lower limit of this range as initiated by the reduction of  $\text{P}^{5+}$  and other cations as  $\text{Ge}^{4+}$ ,  $\text{Sn}^{4+}$ , etc. in thiophosphates, depending on the exact SE composition.<sup>4,13</sup> As in the case of the  $\text{Li}_{10}\text{GeP}_2\text{S}_{12}$  (LGPS) electrolyte, reaction products can form layers including of electronically conductive components such as Ge or  $\text{Li}_x\text{Ge}$  alloys, and therefore result in continuous electrolyte decomposition and MCI growth.<sup>6</sup> In the case of another important sulfide-based SE, argyrodite-type  $\text{Li}_6\text{PS}_5\text{Cl}$  (LPSCI), electrolyte reduction products are  $\text{Li}_2\text{S}$ ,  $\text{LiCl}$  and  $\text{Li}_3\text{P}$  (assuming full lithiation of phosphorous).<sup>5,12,14,15</sup> Fortunately, the rates of decomposition reactions are kinetically limited for this material due to low partial electronic conductivity of the interphase (i.e., SEI), which grows with the square root of time diffusion kinetics at the anode|SE interface.<sup>16</sup> The impact of this kinetically limited interphase growth on the overall cell resistance is relatively low, particularly as compared to other sulfide-based SEs such as LGPS,  $\text{Li}_6\text{PS}_5\text{I}$ , etc., apparently due to sufficient ionic conductivity of the SEI.<sup>5,10</sup> However, it is very important to consider the long term effects of this interphase growth as the lithium inventory losses and increased resistance will become limiting factors during extended operation of LPSCI-based cells.<sup>5,16</sup> For these reasons, a comprehensive understanding of the chemistry of the growing SEI with advanced characterization is necessary to enable further interface engineering and thus enhance battery performance.<sup>17</sup>

X-ray photoelectron spectroscopy (XPS) is widely used in battery research to characterize the stability of electrode|electrolyte interfaces. The technique enables high surface sensitivity, e.g., with a typical probing depth of 5-10 nm with  $\text{Al-K}\alpha$  radiation (1487.6 eV) when analyzing SEI (consisting of organic and inorganic components) in LiBs.<sup>18</sup> With inorganic materials, the probing depth is even expected to be smaller (e.g.,  $< 6 \text{ nm}$  for

nickel metal).<sup>19</sup> In ASSBs, the SEI is a buried interphase growing between two solid materials making its access/analysis difficult. The most common approach is to perform *post mortem* analysis of samples extracted from cells which were disassembled (ideally in a glovebox) and then subsequently transferred under inert atmosphere into the XPS instrument. Even though this approach can provide quite valuable information, these studies provide only a limited view on the underlying processes. The electrochemical/chemical reactions taking place during cell operation may result in intermediates and products that are only stable during cell operation and thus can easily be missed in *ex situ* studies. Additional side reactions during sample preparation (and transfer) can result in self-discharge reactions which in turn can compromise the drawn conclusions. In case sputter depth profiling is employed to analyze deeper sample regions, the existing chemical environment may be altered due to sputter damage.<sup>20</sup> *In situ* and *operando* experiments offer more accurate information on the kinetics of side reactions and identification of degradation products.<sup>17,18,21–24</sup> The need for additional sample preparation is eliminated, which otherwise may alter chemistry and obscure intermediate reaction mechanisms.

In previous studies, the *in situ* analysis of the lithium metal|sulfide-SE interface has mainly relied on *in situ* deposition of lithium metal on solid electrolyte pellets. In one approach as first reported by Wenzel et al., lithium metal deposition was achieved inside the XPS analysis chamber by sputtering of a lithium metal plate (with  $\text{Ar}^+$  ions) which is appropriately oriented with respect to the SE pellet surface.<sup>25</sup> In an alternative approach, as previously applied to oxide-based SEs,<sup>26,27</sup> lithium vapor deposition was performed inside a preparation chamber attached next to the analysis chamber (thus allowing sample transfer under UHV conditions).<sup>28</sup> In a third approach, lithium was deposited quasi-electrochemically by using the sulfide SE surface as a ‘virtual working electrode’ exposing it to an electron beam (e.g., using an  $\text{e}^-$  flood gun) and leading to build up of negative charge.<sup>28–30</sup> In this approach, the SE pellet was placed on top of an excess lithium counter electrode (e.g., lithium metal) which was electronically grounded to the sample stage. As additional thermal or kinetic energy (via the electron/ion neutralizer, the sputtered  $\text{Li}^+$  ions, etc.) is transferred to the surface of the SE, the actual reactivity of the anode|SE interface and the SEI may be altered.<sup>27,28</sup> Additionally, in all of these approaches, the surface of the SE pellet is immediately exposed to the potential of lithium metal upon its deposition, i.e., 0 V (vs.  $\text{Li}^+/\text{Li}$ ). This is a serious limitation, as spectroscopic information from the potential region notably above 0 V (vs.  $\text{Li}^+/\text{Li}$ ), where electrolyte reduction reactions and SEI growth already start, remains inaccessible. Theoretical calculations show that  $\text{Li}_6\text{PS}_5\text{Cl}$ , e.g., will already suffer from reduction once the potential drops below 1.7 V (vs.  $\text{Li}^+/\text{Li}$ ).<sup>11</sup>

In this study, we adopt a different approach to investigate the electrochemical decomposition of LPSCI SE through an ultrathin metal film as electrode (and current collector) which is partially transparent to the photoelectrons. The idea of using electron-transparent films (e.g., graphene) for probing electrochemical processes has been demonstrated already in earlier studies, both in liquid<sup>31–34</sup> and solid phase<sup>35</sup> cell setups. These methodologies are not easily applicable to sulfide-based SEs due to their sensitivity to film transfer, cleaning or water exposure. In a different approach, Kiuchi *et al.* made use of 10 nm thick aluminum metal films to study LiCoO<sub>2</sub> cathode active material in model-type solid-state thin film cells.<sup>36</sup> Here, we adopt a similar thin metal film approach to study the decomposition of sulfide-based LPSCI SE. The surface of the SE pellet is coated with a thin film of nickel metal (6 nm) acting as a current collector (CC) and thereby as a working electrode (WE). Lithium metal is pressed to the other side of the pellet and used as a counter electrode (CE) and reference electrode (RE). This cell (in so-called “anode-free” configuration, *i.e.*, without initial lithium reservoir) is then placed in a specially designed cell holder and connected to a potentiostat to gradually polarize the WE to controlled potentials (and eventually plate lithium metal electrochemically at 0 V *vs.* Li<sup>+</sup>/Li). We then make use of the high photon energies available at a synchrotron source resulting in higher kinetic energy electrons (compared to when using an in-house XPS setup with Al K<sub>α</sub> excitation at 1486.6 eV), necessary for the analysis of the Ni|LPSCI interface buried under the 6 nm thick nickel CC on an appropriate time scale. This approach allows investigation of electrolyte decomposition reactions at *operating* conditions and a wide range of potentials.<sup>36,37,38</sup>

## Results and Discussion

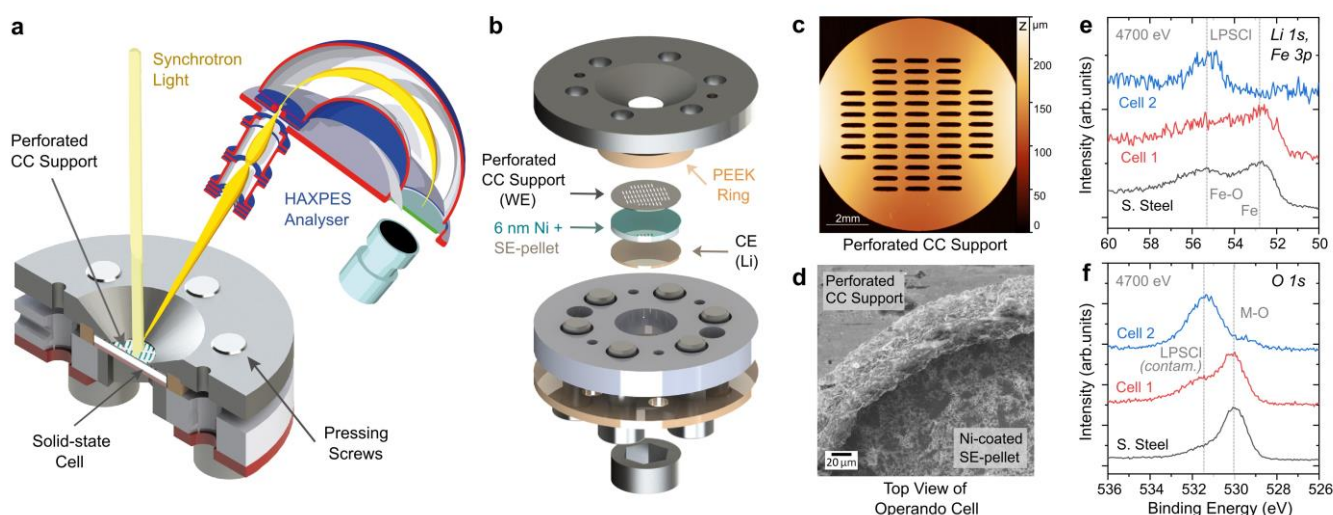


**Figure 1.** (a) Schematic illustration of the operando HAXPES measurement. (b) Close-up illustration of the operando cell. (c) Confocal microscope image of the Ni-coated stainless steel perforated CC support. (d) SEM top view image of the operando cell. (e) Li 1s / Fe 3p and (f) O 1s HAXPES spectra acquired at excitation energy of 4700 eV using the operando cell before (red spectra) and after Ni-coating of the perforated support (blue spectra). Corresponding spectra of the stainless steel are shown for comparison (black spectra).

In the *operando* HAXPES experiment, the bottom side of the LPSCI pellet faced the CE (lithium metal), and the top side faced the WE (6 nm nickel film) and perforated stainless steel CC support as depicted in **Figure 1a-d**. Copper, stainless steel, and nickel are examples of most commonly used CCs for negative electrodes.<sup>37</sup> As shown in a recent study,<sup>16</sup> copper is less stable as compared to nickel and stainless steel when used as a negative electrode CC in contact with sulfide-based SEs. As the film deposition process for stainless steel would be more complicated than for elemental nickel, the latter was chosen as the CC material in this study.

In the cell configuration depicted in **Figure 1a-d**, the electronically conductive nickel film acts as WE on the SE surface, therefore, it needs to form a sufficiently uniform/closed film. This implies that a greater thickness of nickel film is preferable (*i.e.*, for good coverage). On the other hand, since photoelectron spectroscopy is (even when using hard X-rays) a highly surface-sensitive technique, the thickness of this film must also be minimized to allow the detection of electrons emitted from the SE and SEI layers beneath the nickel film. Increasing the incoming photon energy would mitigate this issue as it would result in higher kinetic energy of emitted electrons – and thus an increase in the probing depth of the analysis (*i.e.*, due to higher IMFP of electrons),<sup>38</sup> however, with increasing photon energy the photoionization cross sections will drop significantly. Hence, here, we deposited a nickel film of  $\approx 6$  nm thickness and used an incoming photon energy of 4700 eV as a good compromise to result in high quality data (with sufficient signal-to-noise ratio) in a reasonable measurement time. The optimized sample environment, *i.e.*, nickel film coating of the perforated steel plates and the presence of this perforated CC, did not compromise the

electrochemical performance since the in-house testing of the *operando* cell showed a similar charge/discharge profile during the first cycles of Li plating/stripping as compared to an identical cell prepared without nickel coating but with a thick (2 mm) stainless steel CC (see **Figure S1**).

In addition to the coating of the LPSCl pellet, the stainless steel perforated CC support was also coated with nickel film since the analysis through the small sized slits could cause signals originating from this CC support. Indeed, the first cell we prepared consisted of a non-coated CC support which resulted in overlapping signals originating from the stainless steel in Li 1s / Fe 3p and O 1s regions, and these undesired signals disappeared after nickel coating of the CC support (see **Figure 1e-f**).

**Electrochemical Polarization & Lithium Plating.** The low potential end of the electrochemical stability window of the solid electrolyte was first probed by electrochemical reduction of the SE. Before starting the electrochemical polarization experiment (to low voltages) by the potentiostat, the *operando* cell was kept in the open-circuit state for several hours and the pristine state of the WE was measured as  $\approx 1.94$  V vs.  $\text{Li}^+/\text{Li}$  (unless specified otherwise, all potentials will be referenced vs.  $\text{Li}^+/\text{Li}$  throughout this article). These measurements not only revealed the pristine state of the WE prior to the electrochemical experiment, but also demonstrated the effectiveness of the thin nickel film against beam damage (see **Figure S2** which shows the impact of beam

exposure on LPSCl samples with and without the thin nickel film). During polarization, the applied current was  $10 \mu\text{A}$  (i.e.,  $15.6 \mu\text{A cm}^{-2}$ ). However, in order to facilitate the binding energy calibration and HAXPES data analysis, constant voltage holding periods were maintained during the measurements, thereby resulting in voltage profiles similar to staircase voltammetry experiments (see **Figure 2a**). In order to systematically explore the effect of WE potential on SE decomposition, the potential was gradually decreased to 0.01 V (i.e., just above the Li metal plating potential).

After the polarization experiment, a new electrochemical method which has been recently reported for the SEI quantification, i.e., coulometric titration time analysis (CTTA),<sup>16</sup> was performed with the same *operando* cell to study the impact of decomposition in the presence of lithium metal (see **Figure 2b**). In this particular experiment, lithium was plated on the WE during short pulses (current of  $100 \mu\text{A}$  for  $\approx 7$  seconds) corresponding to a pulse charge of  $0.2 \mu\text{Ah}$ , and the cell was subsequently left in the OCV state until SEI formation had consumed all lithium plated during the pulse. This approach enables the simultaneous quantification of electrolyte reduction reactions while accounting for the presence of the active lithium metal electrode. These pulse/OCV cycles were repeated for a total of approximately 4 hours (i.e.,  $3.4 \mu\text{Ah}$ ) with concurrently performed HAXPES measurements. At the end of this experiment, lithium metal plating and stripping was performed for one cycle (in order to see the impact of

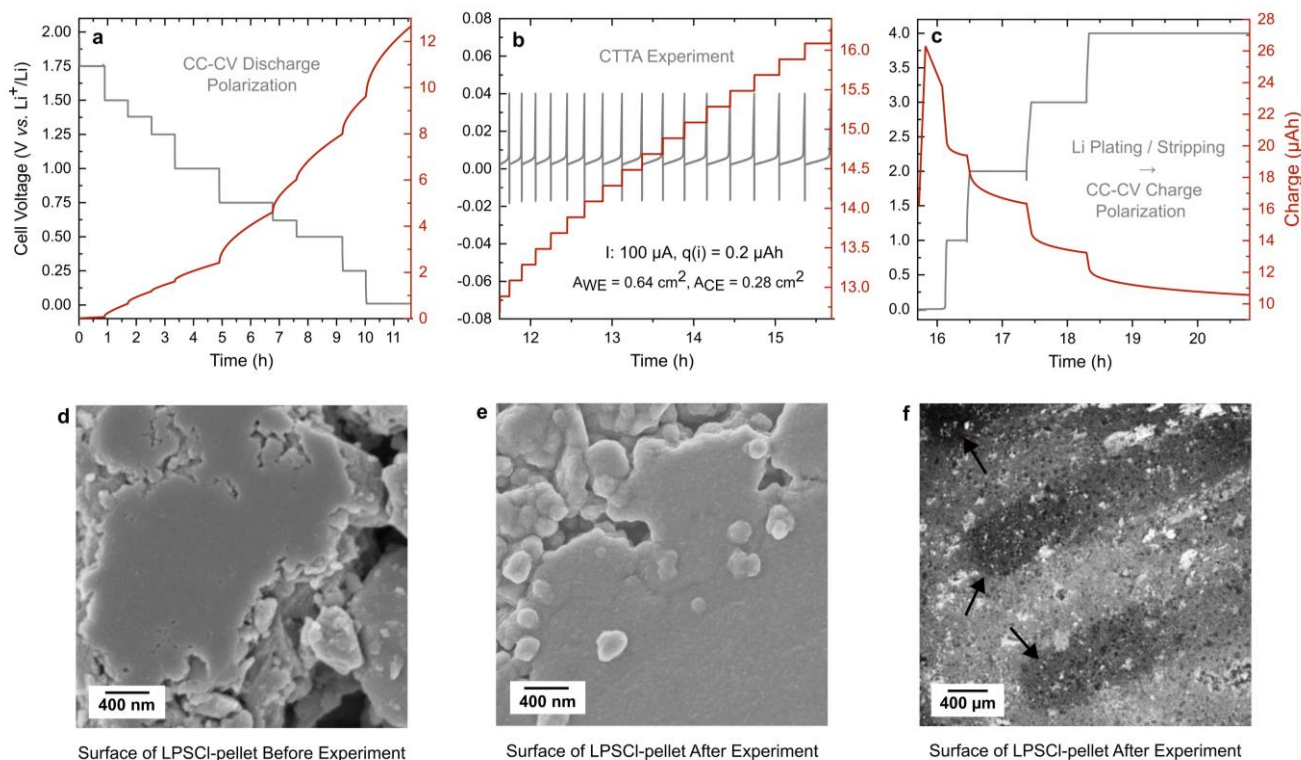


**Figure 2.** (a) Constant current – constant voltage (CC-CV) polarization to lower voltages during the *operando* experiment. This is followed by (b) a CTTA experiment, and later, (c) lithium plating / stripping (one cycle) and CC-CV polarization to higher voltages. SEM images of the LPSCl-pellets (d) before and (e-f) after the *operando* HAXPES experiment.

lithium plating in relatively larger quantities, i.e., at 10  $\mu$ Ah).

The partially reversible nature of electrolyte decomposition in SEs such as LPSCI is well-known,<sup>14,39</sup> and further investigation is crucial to understand the behavior of reduced decomposition products under oxidative conditions (i.e., at high voltages). Therefore, at the end of lithium stripping, the cell was subsequently polarized to high voltages of up to 4 V as shown in **Figure 2c** while acquiring HAXPES at certain potentials.

The morphology of the Ni-coated LPSCI surface (i.e., WE) changed during the *operando* experiment indicating pronounced SEI growth. As shown in **Figure 2d-e**, the initially smooth surface of the WE becomes rougher and develops a thin and planar decomposition layer with a fine microstructure in the areas corresponding to the analysis region (i.e., perforated regions of the current collector disc). These regions are clearly visible in the lower magnification SEM image (see **Figure 2f**), as a contrast shift emerged during the removal of the perforated disc during *post mortem* sample preparation. This shift is mainly attributable to the better adhesion of SEI components<sup>16</sup> to the CC disc (i.e., unperforated regions) which leads to partial removal of SEI. These observations clearly show that SE decomposition initiated at the interface between nickel film and SE on perforated regions during the *operando* experiment, and therefore a meaningful spectroscopic analysis on these regions is possible, which will be discussed in the following sections.

**Solid Electrolyte Reduction.** The *operando* experiments started with the gradual polarization of the WE towards lower potentials as shown in **Figure 2a**. Core-level HAXPES spectra trends during this experiment are shown in **Figure S3**. During the measurement, the thin nickel film was grounded through the HAXPES analyzer aligning its Fermi levels. Hence, the applied voltage at the working electrode is not anticipated to have any impact on the kinetic energy of the emitted electrons and thus corresponding binding energy of surface species (as long as they maintain their initial chemical state and electrical contact to the CC). Indeed, as can be seen in **Figure S3**, this is evident in the case of the Ni 2*p* peaks. However, electronically non-conductive species buried beneath the nickel film experienced shifts in binding energy (BE). Even though such shifts in BE can serve as indicators of changes in the chemical environment, these shifts can also be attributed to the electric potential profile induced by the polarization of the WE. In the case of pure electrostatic nature, the BE shift would be identical to the potential applied. Indeed, it is observed in **Figure S3** and **Figure S4** that the gradual shifts in peaks related to the SE and SEI correspond to the same magnitude of shift in line with the applied voltage to the WE. Similar observations were made in previous *operando* HAXPES studies with thin film WE (Al|LiCoO<sub>2</sub>)<sup>36,40</sup> and XPS studies with composite WEs (LCO/VGCF|LPS, LTO/VGCF|LPS).<sup>22,41,42</sup> To facilitate the analysis of this electrostatic shift and isolate chemical changes, the WE was polarized with potentiostatic holding steps, so that the applied voltage was kept

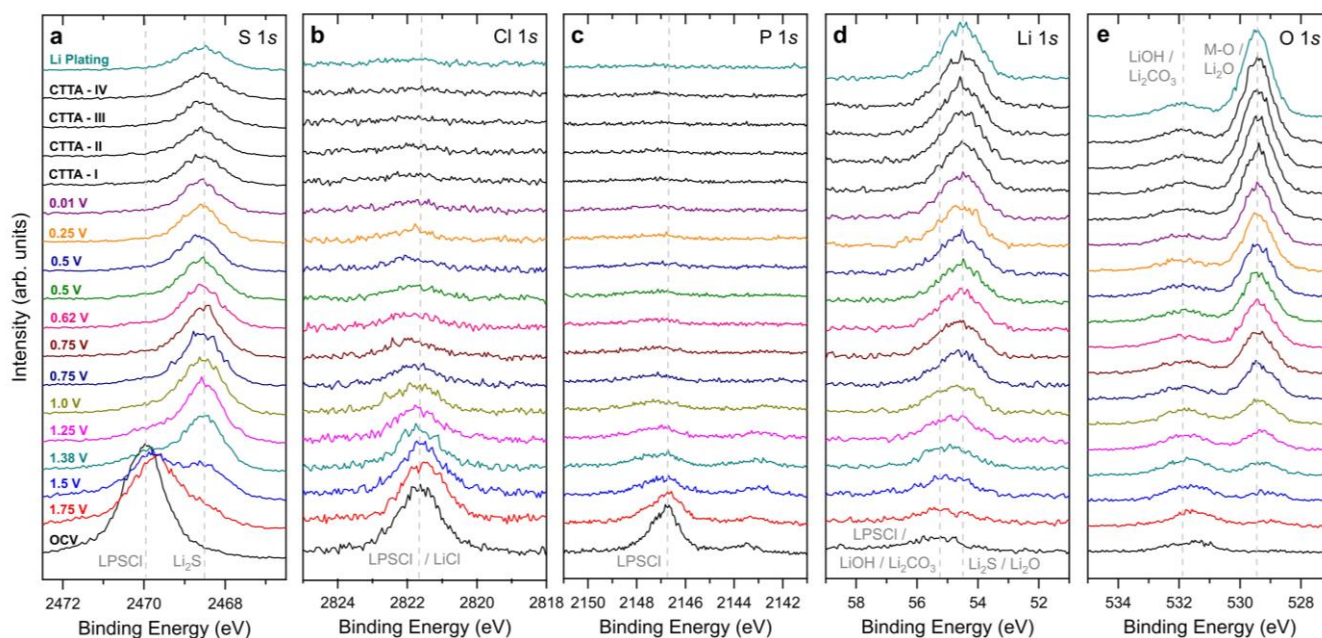


**Figure 3.** Core-level HAXPES spectra observed during the *operando* experiment. The detail spectra showing the electrolyte reduction during gradual polarization (to lower potentials), CTTA and Li plating/stripping are shown in (a) for S 1s, (b) for Cl 1s, (c) for P 1s, (d) for Li 1s, and (e) for O 1s core levels. The photon energy used for these measurements was 4700 eV and no intensity normalization was performed within the data given in each individual graph, however, for better visibility the data was stacked using a constant addend. The vertical dashed lines indicate BE positions of prominent chemical species.

constant during each HAXPES measurement. To compensate for this electrostatic shift a second energy calibration was conducted for each measurement (alongside the initial Au 4*f* calibration). This secondary energy correction procedure involved simply subtracting the difference  $E_{WE,OCV} - E_{WE}$  from the BE for each respective measurement. This calibration approach was chosen as SEI formed in LPSCI SE presumably consists of electronically non-conductive phases. The results of such voltage-corrected spectra obtained during the *operando* experiment are shown in **Figure 3**.

The pristine nickel-covered LPSCI-pellet in OCV state, as expected, contains pure unreacted LPSCI (see **Figure 4** and **Figure S5** for peak fittings at selected WE potentials). Its surface composition is dominated by the prominent peaks in the S 1*s*, Cl 1*s*, and P 1*s* core levels attributed to LPSCI. The small impurities observed include P-S<sub>n</sub>-P and Li<sub>2</sub>S species, usually observed in these compounds as post-synthesis residues.<sup>43,44</sup>

Application of slightly reducing potentials immediately leads to LPSCI decomposition and pronounced SEI formation. Already upon polarization to  $E_{WE} = 1.75$  V, a significant shoulder at around 2468.5 eV appears in the S 1*s* spectrum, corresponding to Li<sub>2</sub>S formation,<sup>45</sup> which is known to be the main SEI component for LPSCI SE.<sup>16</sup> This peak becomes prominent at  $E_{WE} = 1.5$  V and dominates the whole spectrum at  $E_{WE} = 1$  V

(see **Figure 4** for peak fittings and **Figure S6** for respective residual spectra). It is known from previous studies that the Cl 2*p* peak position does not show a significant shift during electrolyte reduction since LPSCI and LiCl have similar Cl 2*p* binding energies, and therefore are not easily distinguishable in experiments,<sup>5,30</sup> which is also confirmed in this study (see **Figure S5** which shows Cl 2*p* peak shifts less than 0.3 eV). In this case, the trends of the Cl 1*s* (and Cl 2*p*) spectra confirm the reliability of the energy calibration procedure used in this study since the peak positions did not show comparable shifts with respect to the applied WE potential. The main P 1*s* peak at 2146.8 eV diminishes and the surface becomes rather deficient in phosphorus already at  $E_{WE} = 1.5$  V (similar trends are also observed in **Figure S5b** for the P 2*p* spectra despite the higher kinetic energy and thus probing depth at this core level).

The intensity trend of each core level is shown in **Figure 4d** with respect to their intensities in the OCV state. Except O 1*s* and Li 1*s*, the core levels of the other elements gradually decrease with decreasing WE potential. As seen in **Figure 4e**, the intensity ratio of specific core levels to the sum of all core levels also follows similar trends. The fact that the Ni 2*p* signal intensity also decreases during the experiment indicates that either new species are forming on top of the nickel film, or the nickel film mechanically disintegrates due to volume

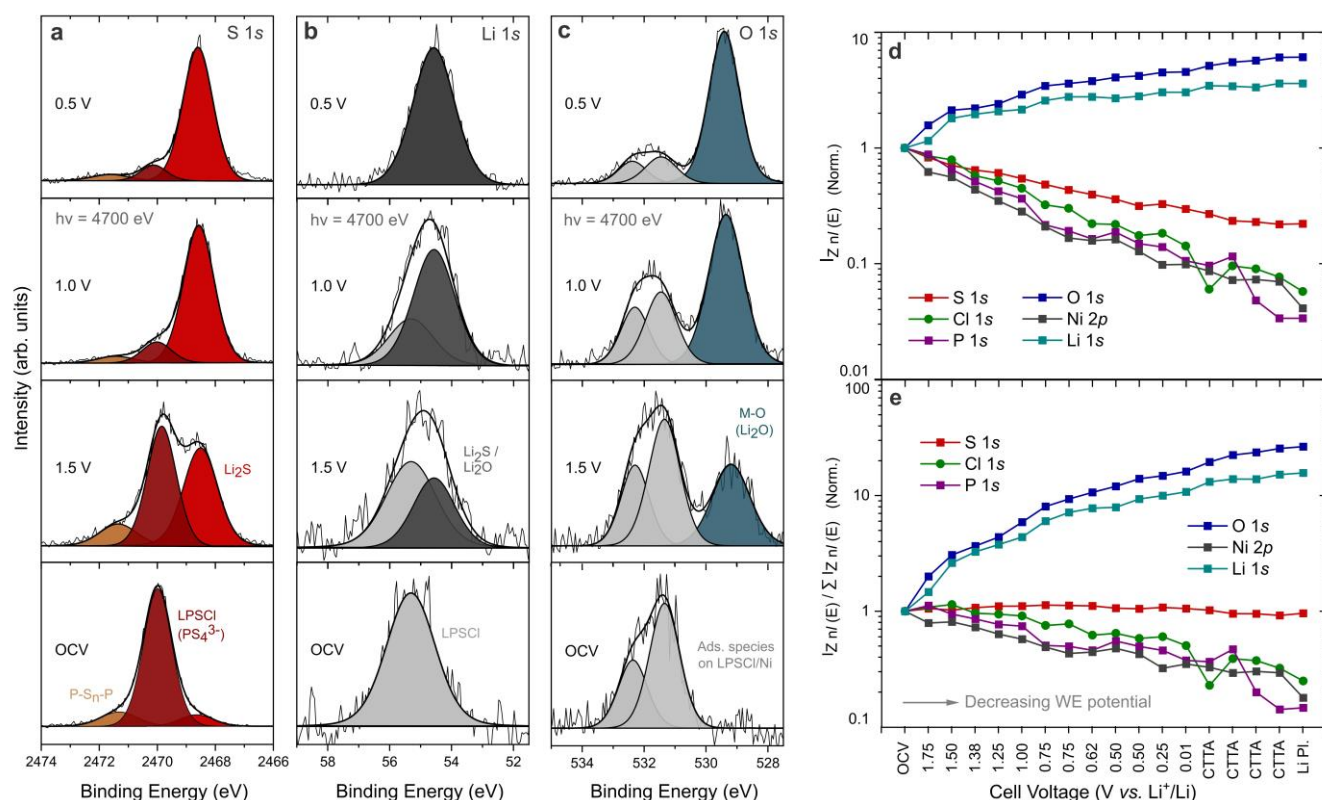


**Figure 4.** Normalized HAXPES detail spectra with peak fittings at selected WE potentials for (a) S 1*s*, (b) Li 1*s*, and (c) O 1*s* core levels. (d) The change of intensity (i.e., total area) with  $E_{WE}$  for each core level as normalized to the intensity before the start of experiments (i.e., OCV-state). (e) The ratio of the specific core-level intensity to the sum of the intensities for all core levels as normalized to the ratio before the start of experiments (i.e., OCV-state).

changes associated with the side reactions and SEI growth. However, as shown in **Figure S3**, the Ni 2p peak position remains almost constant with decreasing  $E_{WE}$  which is an indication of an intact electronic network on the surface throughout the experiment (the possibility of Ni film oxidation by residual oxygen is similarly ruled out). This indicates that oxygen and lithium containing compounds may deposit on top of the nickel film. Such a deposition would rely on electrochemical reduction, thereby necessitating an electronic and ionic conduction pathway and thus the deposition of these species between the nickel film and the electrolyte, which could partially cause film fracture. However, considering the fact that this nickel film is only about 6 nm, it should also be considered that lithium ions may diffuse through nickel,<sup>46</sup> and form oxygen and lithium containing deposits on top of this thin nickel film. It should be noted that the electrolyte has no intentional oxygen in its composition, however, residual oxygen present on SE, in cell components, and in the analysis chamber can contribute to the formation of oxygen-containing compounds – as well known from previous XPS studies.<sup>25,29,47</sup>

Oxygen build-up in the SEI is further confirmed by detailed analysis of Li 1s photoemission spectra. The fitted Li 1s spectra at selected potentials confirm the formation of a new peak corresponding to binding energies of Li<sub>2</sub>S and Li<sub>2</sub>O. The formation of Li<sub>2</sub>S is clearly visible in the S 1s spectra, and therefore a corresponding new peak in the Li 1s spectra is expected. However, as can be seen in **Figure 4c**, the formation of a strong metal oxide peak at  $\approx 529.4$  eV is already visible at  $E_{WE} = 1.5$  V, and this new peak gets more intense upon further decrease of the  $E_{WE}$ . Considering the similar intensity trends of O 1s and Li 1s in **Figure 4d-e**, this new peak appearing in the Li 1s spectra is mainly attributed to Li<sub>2</sub>O formation (with a relatively smaller contribution from Li<sub>2</sub>S). In an earlier study, preferential formation of an oxygen-rich planar film near the stainless steel current collector was demonstrated with a combined *post mortem* analysis (via XPS, SEM-EDS and secondary ion mass spectrometry) of LPSCI-based cells.<sup>16</sup> In this study, similar observations are readily confirmed from the BE positions and overall intensity trends, highlighting the *operando* experiment's practical value. As can be seen in **Figure S7**, *post mortem* SEM-EDS analysis also revealed the presence of oxygen-rich spherical particles, consistent with findings of our previous study.<sup>16</sup> In another study performed under UHV conditions, formation of heterogeneous oxygen-rich SEI components (e.g. Li<sub>2</sub>O) was shown to form also for another SE (i.e., LPS),<sup>29</sup> and these findings highlight that the role of oxygen at low (reducing) potentials remains significant for sulfide-based SEs even under UHV environments.

It has been reported in previous studies that the SEI forming at the Li|LPSCI interface develops a layered microstructure with preferential Li<sub>2</sub>S formation near the lithium metal side as compared to other SEI components such as LiCl and Li<sub>3</sub>P which are preferentially formed

near the SE pellet side.<sup>16,48,49</sup> In the present *operando* HAXPES experiment, despite the absence of lithium metal (i.e., at potentials above  $E_{WE} = 0$  V), the preferential Li<sub>2</sub>S formation is similarly observed and it can clearly be seen in the intensity trends given in **Figure 4a** and **Figure 4d-e**. Furthermore, as seen in **Figure 3**, **Figure 4d-e** and **Figure S5**, the distribution of Cl-rich and P-rich components within the SEI also exhibits a preference since the depletion rate of phosphorus is higher as compared to chlorine during the initial stages of SEI growth (e.g., at  $E_{WE} = 1$  V).

In the preceding sections, the discussion has focused on electrolyte decomposition reactions (i.e., reduction reactions) and SEI formation at relatively high potentials ( $0.01 < E_{WE}/V < 2$ ), i.e., prior to lithium plating. However, after the CC-CV discharge polarization experiment, lithium plating was also performed. Either small amounts of lithium (corresponding to 0.2  $\mu$ Ah) were repeatedly plated with OCV intervals between each plating step (i.e., using the CTTA method),<sup>16</sup> or lithium was plated in a single step with a larger amount of charge (10  $\mu$ Ah). The general trends visible in **Figure 3** and **Figure 4d-e** show that the lithium plating results in an increase (or decrease) of peaks that had already evolved during the polarization experiment, indicating no change in the reaction products but rather a change in the reaction kinetics. Interestingly, as seen in **Figure 3d** and **Figure S8**, the Li 1s peak retains its peak shape and position but shows an increase in intensity upon lithium plating. This suggests that the HAXPES analysis area or the perforated electrode regions did not align well with the spots that are favorable for lithium metal nucleation (alternatively, the SEI formation proceeded faster than Li plating, or the plating occurred below the existing SEI). The characteristic broad plasmon peak of lithium metal (see **Figure S8b**) was also absent. Nevertheless, the plated lithium metal was corroded by the SE present at the analysis area, leading to further SEI growth through alternative galvanic pathways on the sample surface (e.g., electron conduction through the nickel film and ion conduction through the solid electrolyte).

So far, we have shown that *operando* HAXPES, with its high sensitivity and ability to monitor region near the CC at various electrode potentials, is a useful experimental approach for tracking SE reduction and SEI formation. It not only allows for the identification of SEI products but also provides insights into the heterogeneous/layered microstructure of the SEI. In a second step, we also explored the reversibility of SEI-forming reactions. It is known that reduction products of sulfide-based SEs can be oxidized back to LPS-like phases if the electrode potential is raised again, offering a certain degree of reversibility to the charge consumed in decomposition reactions.<sup>14,39</sup> For this reason, at the end of Li stripping,  $E_{WE}$  was gradually increased back to higher potentials in order to investigate the onset and course of SEI (and SE) oxidation reactions.

**Oxidation of SEI and SE.** In order to investigate the reversibility of SE reduction reactions, the *operando* cell was subsequently and gradually polarized to  $E_{WE} = 1$  V, 2 V, 3 V and 4 V. The fitted spectra are shown in **Figure 5** and respective residual spectra in **Figure S9** (spectra at 0 V and 1 V were similar and thus only the latter is shown). At  $E_{WE} = 1$  V, the S 1s spectrum does not show any considerable change except the appearance of a rather weak peak at  $E_B \approx 2476.7$  eV which can be attributed to sulfite-like species.<sup>50</sup> This peak exhibits a slight increase in intensity at  $E_{WE} = 2$  V vs.  $Li^+/Li$ . However, a more prominent peak at  $E_B = 2479.2$  eV (attributed to sulfate-like species based on  $E_B$  shift observed in S 2p in earlier studies<sup>51–53</sup>) emerges at this potential and gradually intensifies at  $E_{WE} = 3$  V, and a further increase in intensity occurs when the potential is increased to  $E_{WE} = 4$  V. The intensity of this peak follows a trend opposite to that of the intensity of the  $Li_2S$  peak, suggesting its formation through oxidative decomposition of  $Li_2S$ . Additionally, a new peak at 2472.1 eV also appears at high potentials. This peak is attributed to elemental sulfur and oxidized sulfur species (polysulfides with the general formula  $Li_2S_n$ ) which have been reported to form during cycling of cathode composites consisting of sulfide-based SEs.<sup>14,39,43,44</sup>

It is seen from the intensity trends in **Figure 5d-e** that oxygen, and particularly lithium fractions at the surface, rapidly decrease at potentials above  $E_{WE} = 2$  V. This is mainly caused by the oxidation of  $Li_2O$  as can be

seen in **Figure 5c**. Two main peaks in the O 1s spectra become rather visible at  $E_{WE} = 2$  V, in parallel with the formation of sulfites/sulfates as observed in the S 1s spectra, and thus we associate the O 1s components with the same species. Interestingly, intensity trends of these species do not exactly match each other in the O 1s and S 1s spectra, indicating a heterogeneity in the SEI microstructure, with sulfites tending to be located deeper in the bulk of SEI. The Ni 2p spectrum (see **Figure S10**) shows some changes, particularly at  $E_{WE} = 4$  V, indicating that the nickel film also appears to take part in oxidation reactions at this potential (e.g., sulfate formation).<sup>54</sup> The probing depth in the O 1s core level is higher than the S 1s core level due to differences in electron kinetic energies (*i.e.*, 4170 eV vs. 2230 eV, respectively), highlighting the possibility of utilizing HAXPES (even with fixed excitation energy) for studying such layered systems. At the end of the electrolyte oxidation experiment, the cell was abruptly brought below 0 V, and lithium metal was deposited in order to check the reversibility of electrolyte oxidation reactions. The measurements were performed after lithium deposition (*i.e.*, at OCV) and the results show a strong reversal of lithium intensity trends (**Figure 5e**) and reappearance of strong  $Li_2S$  and  $Li_2O$  peaks in the S 1s and Li 1s spectra. Remarkably, the binding energy position of the  $Li_2O$ -related peak shifted slightly towards lower energies, suggesting some alterations within the SEI microstructure during the oxidation-reduction cycle. This could be due to changes in the

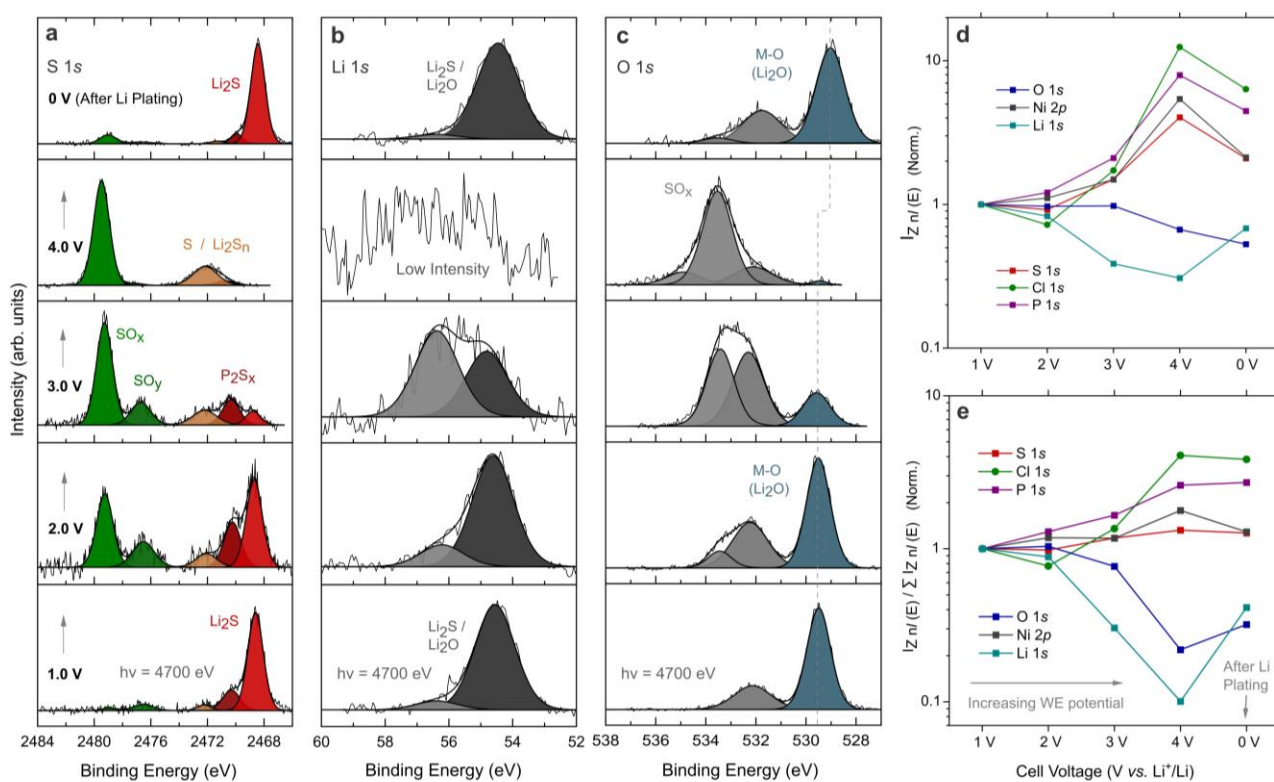


**Figure 5.** Normalized HAXPES detail spectra evolution during polarization to high potentials with peak fittings for (a) S 1s, (b) Li 1s, and (c) O 1s core levels. (d) The change of intensity (*i.e.*, total area) with WE potential for each core level as normalized to the intensity at 1 V. (e) The ratio of specific core level intensity to the sum of intensities for all core levels as normalized to the ratio at 1 V.

location of freshly formed  $\text{Li}_2\text{O}$  with respect to the electronically conductive nickel film (e.g., thus due to alterations in the differential charging effects).

## Conclusions

*Operando* HAXPES experiments were performed on sulfide-based  $\text{Li}_6\text{PS}_5\text{Cl}$  solid electrolyte to monitor and understand its reduction reactions upon lithiation and resulting SEI growth. A thin nickel film ( $\approx 6$  nm) was used as a partially photoelectron-transparent current collector/working electrode to control the electrode potential (and current) by the external potentiostat. The use of high photon energies in HAXPES measurements enables the dynamic investigation of the buried interphase formed below the nickel film.

The stability window of sulfide-based SEs is known to be rather narrow, and our work confirms that reduction already starts at potentials as high as  $E_{\text{WE}} = 1.75$  V vs.  $\text{Li}^+/\text{Li}$ , in agreement with theory.<sup>11</sup> Side reactions result in significant  $\text{Li}_2\text{S}$  formation in the potential window of 1.5 – 1.0 V vs.  $\text{Li}^+/\text{Li}$ . With decreasing potential, the change of intensity follows distinct trends for different elements. The relative intensity of lithium increases as SE reduction progresses. This is partly due to  $\text{Li}_2\text{S}$  formation, but more prominently due to  $\text{Li}_2\text{O}$  formation, indicating the involvement of trace-oxygen in side reactions. The overall intensity trends suggest that the SEI has a heterogeneous/layered microstructure with  $\text{Li}_2\text{O}$  preferentially located near the current collector, followed by  $\text{Li}_2\text{S}$ . Additionally, with decreasing potential, regions near the current collector become increasingly deficient in chlorine and, even more so, in phosphorus. Theoretical work is already run to model the underlying reaction mechanisms,<sup>12,55–58</sup> and we are confident that our approach will be a highly valuable source of experimental data.

The *operando* HAXPES experiments have also proven to be useful in studying the reversibility of decomposition reactions. Upon increasing the potential, within the 2 - 4 V vs.  $\text{Li}^+/\text{Li}$  potential window,  $\text{Li}_2\text{O}$  and  $\text{Li}_2\text{S}$  are gradually oxidized to form sulfite and sulfate species, along with oxidized sulfur species (polysulfides). It is shown that these species convert back to the same major SEI components upon subsequent Li plating. This demonstrates that our experimental approach is able to monitor and quantify reversible and irreversible SE decomposition reactions under dynamic and practically relevant conditions.

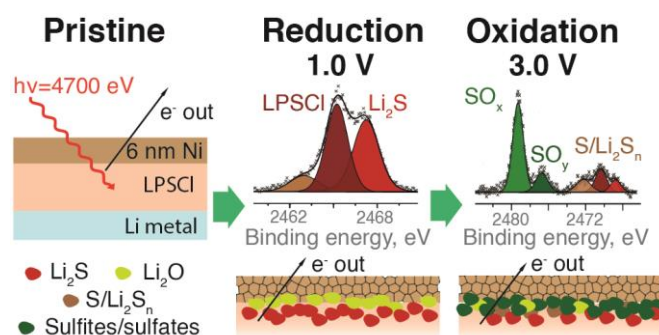
**Author contributions.** B.A. and E.K. contributed equally to this work. B.A. wrote the manuscript, performed data analysis, and conducted in-house electrochemical experiments. E.K. designed the custom-built *operando* cell and provided input to the manuscript. E.K., B.A., L.R., R.G.-D., Z.C., J.B., R.G.W. took active role in experiments and HAXPES measurements. R.G.W. and M.B. advised on HAXPES data evaluation. J.B.

and B.A. performed SEM/EDS measurements, and J.B. performed confocal microscope imaging. All authors read the manuscript, provided feedback, and contributed to this study with useful discussions.

**Acknowledgements.** The authors are grateful to the Energy Materials In-Situ Laboratory (EMIL) at BESSY II for access to synchrotron radiation beamtime that enabled the HAXPES experiments. B.A. acknowledges funding from the Bundesministerium für Bildung und Forschung (BMBF) within the FestBatt – Cluster of Competence for Solid-State Batteries (FB2-Char 03XP0433D, FB2-Thio 03XP0430A). E.K. acknowledges funding by the BMBF in the framework of the operaXX project (03XP0328A). The authors thank Johannes Frisch and Tzung-En Hsieh for the help with the deposition of Ni thin films. R.G.-D. acknowledges funding by the BMBF in the framework of the CatLab project (03EW0015A/B). For support of optimizing the CPMU17 EMIL beamline for HAXPES measurements we are grateful for A. Efimenko and M. Gorgoi from the Interface Department of HZB. The authors are grateful to Katherine Mazzio and Nazia Nazer (Humboldt University Berlin) for the help in designing of *operando* electrochemical cell.

**Data Availability.** The raw data of experiments is available at doi.org/10.5281/zenodo.10966160.

## TOC Figure.



## References

1. Li, W., Erickson, E. M. & Manthiram, A. High-nickel layered oxide cathodes for lithium-based automotive batteries. *Nat Energy* **5**, 26–34 (2020).
2. Frith, J. T., Lacey, M. J. & Ulissi, U. A non-academic perspective on the future of lithium-based batteries. *Nat Commun* **14**, 420 (2023).
3. Janek, J. & Zeier, W. G. Challenges in speeding up solid-state battery development. *Nat Energy* **8**, 230–240 (2023).
4. Xiao, Y. *et al.* Understanding interface stability in solid-state batteries. *Nat Rev Mater* **5**, 105–126 (2020).

5. Wenzel, S., Sedlmaier, S. J., Dietrich, C., Zeier, W. G. & Janek, J. Interfacial reactivity and interphase growth of argyrodite solid electrolytes at lithium metal electrodes. *Solid State Ion* **318**, 102–112 (2018).
6. Wenzel, S. *et al.* Direct Observation of the Interfacial Instability of the Fast Ionic Conductor Li<sub>10</sub>GeP<sub>2</sub>S<sub>12</sub> at the Lithium Metal Anode. *Chemistry of Materials* **28**, 2400–2407 (2016).
7. Li, S. *et al.* A Dynamically Stable Mixed Conducting Interphase for All-Solid-State Lithium Metal Batteries. *Advanced Materials* **36**, (2024).
8. Riegger, L. M. *et al.* Instability of the Li<sub>7</sub>SiP<sub>8</sub>S<sub>8</sub>Solid Electrolyte at the Lithium Metal Anode and Interphase Formation. *Chemistry of Materials* **34**, 3659–3669 (2022).
9. Aktekin, B. *et al.* Understanding the Capacity Loss in LiNi<sub>0.5</sub>Mn<sub>1.5</sub>O<sub>4</sub>-Li<sub>4</sub>Ti<sub>5</sub>O<sub>12</sub> Lithium-Ion Cells at Ambient and Elevated Temperatures. *The Journal of Physical Chemistry C* **122**, 11234–11248 (2018).
10. Riegger, L. M. *et al.* Evolution of the Interphase between Argyrodite-Based Solid Electrolytes and the Lithium Metal Anode—The Kinetics of Solid Electrolyte Interphase Growth. *Chemistry of Materials* **35**, 5091–5099 (2023).
11. Zhu, Y., He, X. & Mo, Y. Origin of Outstanding Stability in the Lithium Solid Electrolyte Materials: Insights from Thermodynamic Analyses Based on First-Principles Calculations. *ACS Appl Mater Interfaces* **7**, 23685–23693 (2015).
12. Schwietert, T. K. *et al.* Clarifying the relationship between redox activity and electrochemical stability in solid electrolytes. *Nat Mater* **19**, 428–435 (2020).
13. Richards, W. D., Miara, L. J., Wang, Y., Kim, J. C. & Ceder, G. Interface Stability in Solid-State Batteries. *Chemistry of Materials* **28**, 266–273 (2016).
14. Tan, D. H. S. *et al.* Elucidating Reversible Electrochemical Redox of Li<sub>6</sub>PS<sub>5</sub>Cl Solid Electrolyte. *ACS Energy Lett* **4**, 2418–2427 (2019).
15. Cheng, T., Merinov, B. V., Morozov, S. & Goddard, W. A. Quantum Mechanics Reactive Dynamics Study of Solid Li-Electrode/Li<sub>6</sub>PS<sub>5</sub>Cl-Electrolyte Interface. *ACS Energy Lett* **2**, 1454–1459 (2017).
16. Aktekin, B. *et al.* SEI growth on Lithium metal anodes in solid-state batteries quantified with coulometric titration time analysis. *Nat Commun* **14**, 6946 (2023).
17. Zhao, F., Zhang, S., Li, Y. & Sun, X. Emerging Characterization Techniques for Electrode Interfaces in Sulfide-Based All-Solid-State Lithium Batteries. *Small Struct* **3**, 2100146 (2022).
18. Maibach, J., Rizell, J., Matic, A. & Mozhzhukhina, N. Toward *Operando* Characterization of Interphases in Batteries. *ACS Mater Lett* **5**, 2431–2444 (2023).
19. Tanuma, S., Powell, C. J. & Penn, D. R. Calculations of electron inelastic mean free paths. V. Data for 14 organic compounds over the 50–2000 eV range. *Surface and Interface Analysis* **21**, 165–176 (1994).
20. Andersson, A. M., Henningson, A., Siegbahn, H., Jansson, U. & Edström, K. Electrochemically lithiated graphite characterised by photoelectron spectroscopy. In *Journal of Power Sources* vols 119–121 522–527 (2003).
21. Narayanan, S., Gibson, J. S., Aspinall, J., Weatherup, R. S. & Pasta, M. In situ and operando characterisation of Li metal – Solid electrolyte interfaces. *Curr Opin Solid State Mater Sci* **26**, 100978 (2022).
22. Wu, X., Villevieille, C., Novák, P. & El Kazzi, M. Monitoring the chemical and electronic properties of electrolyte-electrode interfaces in all-solid-state batteries using: Operando X-ray photoelectron spectroscopy. *Physical Chemistry Chemical Physics* **20**, 11123–11129 (2018).
23. Strauss, F. *et al.* Operando Characterization Techniques for All-Solid-State Lithium-Ion Batteries. *Advanced Energy and Sustainability Research* **2**, 2100004 (2021).
24. Boebinger, M. G., Lewis, J. A., Sandoval, S. E. & McDowell, M. T. Understanding Transformations in Battery Materials Using in Situ and Operando Experiments: Progress and Outlook. *ACS Energy Lett* **5**, 335–345 (2020).
25. Wenzel, S., Leichtweiss, T., Krüger, D., Sann, J. & Janek, J. Interphase formation on lithium solid electrolytes - An in situ approach to study interfacial reactions by photoelectron spectroscopy. *Solid State Ion* **278**, 98–105 (2015).
26. Schwöbel, A., Hausbrand, R. & Jaegermann, W. Interface reactions between LiPON and lithium studied by in-situ X-ray photoemission. *Solid State Ion* **273**, 51–54 (2015).
27. Connell, J. G. *et al.* Kinetic versus Thermodynamic Stability of LLZO in Contact with Lithium Metal. *Chemistry of Materials* **32**, 10207–10215 (2020).
28. Gibson, J. S. *et al.* Gently does it!: in situ preparation of alkali metal-solid electrolyte interfaces for photoelectron spectroscopy. *Faraday Discuss* **236**, 267–287 (2022).
29. Wood, K. N. *et al.* Operando X-ray photoelectron spectroscopy of solid electrolyte interphase formation and evolution in Li<sub>2</sub>S-P<sub>2</sub>S<sub>5</sub> solid-state electrolytes. *Nat Commun* **9**, 1–10 (2018).
30. Narayanan, S. *et al.* Effect of current density on the solid electrolyte interphase formation at the lithium|Li<sub>6</sub>PS<sub>5</sub>Cl interface. *Nat Commun* **13**, 7237 (2022).
31. Cameci, M. T., Ulgut, B., Kocabas, C. & Suzer, S. In Situ XPS Reveals Voltage Driven Asymmetric Ion Movement of an Ionic Liquid through the Pores of a Multilayer Graphene Electrode. *Journal of Physical Chemistry C* **122**, 11883–11889 (2018).
32. Velasco-Velez, J. J. *et al.* Photoelectron Spectroscopy at the Graphene-Liquid Interface Reveals the Electronic

- Structure of an Electrodeposited Cobalt/Graphene Electrocatalyst. *Angewandte Chemie International Edition* **54**, 14554–14558 (2015).
33. Kerger, P., Vogel, D. & Rohwerder, M. Electrochemistry in ultra-high vacuum: The fully transferrable ultra-high vacuum compatible electrochemical cell. *Review of Scientific Instruments* **89**, (2018).
  34. Endo, R., Watanabe, D., Shimomura, M. & Masuda, T. In situ X-ray photoelectron spectroscopy using a conventional Al-K $\alpha$  source and an environmental cell for liquid samples and solid-liquid interfaces. *Appl Phys Lett* **114**, (2019).
  35. Inozemtseva, A. I. *et al.* In Situ XPS Studies of Solid Electrolyte Electroreduction Through Graphene Electrode. *J Electrochem Soc* **167**, 110533 (2020).
  36. Kiuchi, H. *et al.* Operando hard X-ray photoelectron spectroscopy of LiCoO<sub>2</sub> thin film in an all-solid-state lithium ion battery. *Electrochem Commun* **118**, 106790 (2020).
  37. Zhu, P. *et al.* A review of current collectors for lithium-ion batteries. *J Power Sources* **485**, 229321 (2021).
  38. Källquist, I. *et al.* Advances in studying interfacial reactions in rechargeable batteries by photoelectron spectroscopy. *J Mater Chem A Mater* **10**, 19466–19505 (2022).
  39. Wang, S. *et al.* Lithium Argyrodite as Solid Electrolyte and Cathode Precursor for Solid-State Batteries with Long Cycle Life. *Adv Energy Mater* **11**, 1–28 (2021).
  40. Hikima, K. *et al.* Operando analysis of electronic band structure in an all-solid-state thin-film battery. *Commun Chem* **5**, 52 (2022).
  41. Wu, X., Villevieille, C., Novák, P. & El Kazzi, M. Insights into the chemical and electronic interface evolution of Li<sub>4</sub>Ti<sub>5</sub>O<sub>12</sub> cycled in Li<sub>2</sub>S-P<sub>2</sub>S<sub>5</sub> enabled by: Operando X-ray photoelectron spectroscopy. *J Mater Chem A Mater* **8**, 5138–5146 (2020).
  42. Wu, X., Mirolo, M., Vaz, C. A. F., Novák, P. & El Kazzi, M. Reactivity and Potential Profile across the Electrochemical LiCoO<sub>2</sub>-Li<sub>3</sub>PS<sub>4</sub> Interface Probed by Operando X-ray Photoelectron Spectroscopy. *ACS Appl Mater Interfaces* **13**, 42670–42681 (2021).
  43. Auvergniot, J. *et al.* Redox activity of argyrodite Li<sub>6</sub>PS<sub>5</sub>Cl electrolyte in all-solid-state Li-ion battery: An XPS study. *Solid State Ion* **300**, 78–85 (2017).
  44. Walther, F. *et al.* Influence of Carbon Additives on the Decomposition Pathways in Cathodes of Lithium Thiophosphate-Based All-Solid-State Batteries. *Chemistry of Materials* **32**, 6123–6136 (2020).
  45. Liang, J. *et al.* An Air-Stable and Dendrite-Free Li Anode for Highly Stable All-Solid-State Sulfide-Based Li Batteries. *Adv Energy Mater* **9**, 1902125 (2019).
  46. Evmenenko, G. *et al.* Lithiation of multilayer Ni/NiO electrodes: criticality of nickel layer thicknesses on conversion reaction kinetics. *Physical Chemistry Chemical Physics* **19**, 20029–20039 (2017).
  47. Steinberger, R. *et al.* Oxygen accumulation on metal surfaces investigated by XPS, AES and LEIS, an issue for sputter depth profiling under UHV conditions. *Appl Surf Sci* **411**, 189–196 (2017).
  48. Otto, S. K. *et al.* In Situ Investigation of Lithium Metal–Solid Electrolyte Anode Interfaces with ToF-SIMS. *Adv Mater Interfaces* **2102387**, (2022).
  49. Luo, S. *et al.* Nanostructure of the Interphase Layer between a Single Li Dendrite and Sulfide Electrolyte in All-Solid-State Li Batteries. *ACS Energy Lett* **7**, 3064–3071 (2022).
  50. Zillner, J. *et al.* The Role of SnF<sub>2</sub> Additive on Interface Formation in All Lead-Free FASnI<sub>3</sub> Perovskite Solar Cells. *Adv Funct Mater* **32**, (2022).
  51. Fantauzzi, M., Elsener, B., Atzei, D., Rigoldi, A. & Rossi, A. Exploiting XPS for the identification of sulfides and polysulfides. *RSC Adv* **5**, 75953–75963 (2015).
  52. Wang, C. *et al.* Deciphering Interfacial Chemical and Electrochemical Reactions of Sulfide-Based All-Solid-State Batteries. *Adv Energy Mater* **11**, (2021).
  53. Auvergniot, J. *et al.* Interface Stability of Argyrodite Li<sub>6</sub>PS<sub>5</sub>Cl toward LiCoO<sub>2</sub>, LiNi<sub>1/3</sub>Co<sub>1/3</sub>Mn<sub>1/3</sub>O<sub>2</sub>, and LiMn<sub>2</sub>O<sub>4</sub> in Bulk All-Solid-State Batteries. *Chemistry of Materials* **29**, 3883–3890 (2017).
  54. Nesbitt, H. W., Legrand, D. & Bancroft, G. M. Interpretation of Ni2p XPS spectra of Ni conductors and Ni insulators. *Phys Chem Miner* **27**, 357–366 (2000).
  55. Ren, F. *et al.* Visualizing the SEI formation between lithium metal and solid-state electrolyte. *Energy Environ Sci* (2024) doi:10.1039/D3EE03536K.
  56. Chaney, G., Golov, A., van Rookeghem, A., Carrasco, J. & Mingo, N. Two-step growth mechanism of the solid electrolyte interphase in argyrodite/Li-metal contacts. *arXiv preprint arXiv:2402.04095* (2024).
  57. Golov, A. & Carrasco, J. Unveiling Solid Electrolyte Interphase Formation at the Molecular Level: Computational Insights into Bare Li-Metal Anode and Li<sub>6</sub>PS<sub>5</sub>-xSexCl Argyrodite Solid Electrolyte. *ACS Energy Lett* **8**, 4129–4135 (2023).
  58. Wang, C., Aoyagi, K., Aykol, M. & Mueller, T. Ionic Conduction through Reaction Products at the Electrolyte-Electrode Interface in All-Solid-State Li+Batteries. *ACS Appl Mater Interfaces* **12**, 55510–55519 (2020).